ChemComm

COMMUNICATION

View Article Online
View Journal | View Issue

Cite this: *Chem. Commun.*, 2023, 59, 11795

Received 21st July 2023,
Accepted 7th September 2023

DOI: 10.1039/d3cc03477a

rsc.li/chemcomm

Broadband red emission from one-dimensional hexamethonium lead bromide perovskitoid†

Biqi He,[a] Kuan Kuang,[a] Bing Xu,[b] Junjie Tang,[a] Sheng Cao,[a] Zixian Yu,[a] Mingkai Li,*[a] Yunbin He *[a] and Junnian Chen*[a]

Broadband emissions from low-dimensional hybrid perovskites have aroused intense interest. However, the achievement of broadband red emission in lead halide perovskites remains challenging. Herein, we report a one-dimensional (1D) hybrid lead bromide perovskitoid, (HM)Pb_2Br_6 (HM = hexamethonium), featuring a corrugated "3 × 3" $[Pb_2Br_6]^{2-}$ chain. The unique structure results in intriguingly red emission peaking at 692 nm, with a PLQY of around 6.24%. Our spectroscopic and computational studies reveal that the red emission derives from self-localized Pb_2^{3+}, Pb^{3+} and Br_2^- species confined within the inorganic lead bromide lattice that function as radiative centres. This finding will benefit the design of perovskite systems for efficient red emission.

Hybrid lead halide perovskites have emerged as outstanding semiconductors because of their superb optoelectronic and light emitting performances.[1–3] Notably, their low formation energies[4] and soft crystal nature[5] allow high structural freedom that enables exceptional structure tunability. Actually, the structural dimensionality, more precisely the connectivity of the metal halide octahedra, can be modulated from three-dimensional (3D) to two-dimensional (2D) and one-dimensional (1D) *via* choosing suitable bulk organic cations.[6–8] The dimensionality decrease further yields quantum well structures and a concomitant exciton confinement effect, yielding intriguing light emission properties.[9,10]

Recently, low-dimensional perovskite broadband emitters have aroused intense interest in the solid-state lighting field.[11–14] For instance, Karunadasa *et al.* firstly reported warm white-light emission in 2D (N-MEDA)[$PbBr_4$] (N-MEDA = *N*1-methylethane-1,2-diammonium), which achieved a stable photoluminescence quantum yield (PLQY) of 9%.[15] Mechanism study indicates that the broadband emission stems from the excited-state structural deformation.[16] The 1D $C_4N_2H_{14}PbBr_4$ reported by Ma *et al.* has the [$PbBr_4$] chains composed of double edge-shared octahedral units, which enabled efficient bluish white-emission with a PLQY of 20%.[17] Notably, the development of perovskite red light emitters has extended their application into food quality detection and health monitoring fields.[18,19] Nevertheless, the reported alloy perovskites suffer from phase segregation. Intriguingly, Kovalenko *et al.* presented 2D $[CH(NH_2)_2][C(NH_2)_3]PbI_4$ exhibiting puckered lead-iodide layers, which yielded broadband red luminescence with a PLQY of 3.5%.[20] Besides, 2D $[C_{10}H_{16}N]_4Pb_3Br_{10}$ reported by Zhang *et al.* has the inorganic layer comprised of face-sharing and corner-sharing octahedra, which gained red emission with a PLQY of 2.53%.[21] Moreover, 1D (*N*-fluoroethyl-*N*-methylmorpholine) $PbBr_3$ is shown to exhibit a red emission with CIE chromaticity coordinates of (0.56, 0.42).[22] Unfortunately, the exploration of efficient single-component lead halide perovskite red emitters remains challenging.

Herein, we adopt $(HM)^{2+}$ to template 1D (HM)Pb_2Br_6, which features a corrugated "3 × 3" chain structure composed of face-sharing octahedra. This leads to distinctive short Pb–Pb and Br–Br pairs, and high structure deformation. It displays broadband red emission peaking at 692 nm with a large Stokesshift of 302 nm and a PLQY of around 6.24%. Mechanistic investigation reveals that the red emission has contributions from the self-trapped Pb_2^{3+}, Pb^{3+}, and Br_2^- sites.

The bulk (HM)Pb_2Br_6 single crystals were grown from the precursor solution as a colorless prism (Fig. S1, ESI†). Single-crystal X-ray diffraction (SCXRD) analysis reveals that the (HM)Pb_2Br_6 crystallizes in the monoclinic space group *P*2/*c*. There exists a twofold axis on Pb1 and Pb3 paralleling to the b axis in the $[Pb_2B_6]^{2-}$ inorganic framework. The detailed crystallographic information is recorded in Tables S1–S3 (ESI†). As shown in Fig. 1a, the chain structure is formed with a face-sharing octahedron displaying a roof-like 3 × 3 corrugation, differing from the reported 1D perovskites.[23] Specifically, the

[a] *Ministry-of-Education Key Laboratory of Green Preparation and Application for Functional Materials, and School of Materials Science & Engineering, Hubei University, Wuhan 430062, China*

[b] *Lingnan Normal University, Zhanjiang, 524048, China*

† Electronic supplementary information (ESI) available: Detailed experimental materials and characterizations. CCDC 2266716. For ESI and crystallographic data in CIF or other electronic format see DOI: https://doi.org/10.1039/d3cc03477a

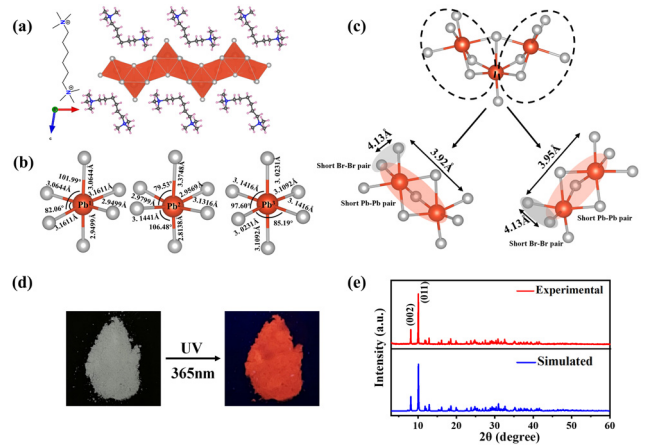

Fig. 1 (a) Crystal structure of (HM)Pb_2Br_6. (b) The Pb–Br bond lengths and Br–Pb–Br bond angles of three individual polyhedra. (c) The detailed view of the Pb–Pb and Br–Br pair distance determined from the SCXRD analysis. (d) Photographs of (HM)Pb_2Br_6 single crystals under ambient light (left) and UV 365 nm light (right). (e) The experimental and simulated XRD patterns of (HM)Pb_2Br_6.

$(HM)^{2+}$ without a H-bond donor and high steric hindrance bonds loosely to the bromide anion to form weak electrostatic interaction and adopts a bending configuration, leading to the inorganic chain folding and resulting in a roof-like 3 × 3 corrugation (Fig. S2, ESI†). Seen from Fig. 1b, the basic building unit consists of three face-sharing octahedra, with the Pb–Br bond lengths ranging from 2.81 (14) (Pb2) to 3.37 Å (14) (Pb2), and the Br–Pb–Br bond angles ranging from 82.06 (3) (Pb1) to 178.60° (4) (Pb3) (Tables S2 and S3, ESI†). The crystal structure has been granted a CCDC number of 2266716.† Besides, the Pb–Pb distances are measured to be 3.92 (Pb3–Pb2) and 3.95 Å (Pb1–Pb2) (Fig. 1c), shorter than that of (TDMP)$PbBr_4$ (4.55 Å).[24] Moreover, the Br–Br distances (4.13 Å) is comparable to that of (TDMP)$PbBr_4$. We then calculated the bond length distortion (Δd) and bond angle variance (σ^2) of the $PbBr_6$ octahedron to assess the structural distortion by using the following eqn (1) and (2).

$$\Delta d = \frac{1}{6}\sum_{n=1}^{6}[(d_n - d_i)]^2 \quad (1)$$

where d_i (or d_n) is the mean (or individual) Pb–Br bond length.

$$\sigma^2 = \frac{1}{11}\sum_{n=1}^{12}(\theta_n - 90^\circ)^2 \quad (2)$$

where θ_n is the individual Br–Pb–Br bond angle. The detailed distortion index is summarized in Table S4 (ESI†). The Δd_{avg} and ${\sigma_{avg}}^2$ are then determined to be 1.49 × 10^{-3} and 48, comparable to the reported perovskite red emitter.[22] The high distortion probably results from the weak organic–inorganic interactions. Intriguingly, the (HM)Pb_2Br_6 single crystals exhibit distinctive red emission upon 365 nm light irradiation (Fig. 1d). The powder XRD matches well with the simulated result, confirming the phase purity of the synthesized crystals (Fig. 1e). The EDS mapping reveals the uniform distribution of Pb and Br elements in the single crystal (Fig. S3, ESI†). The Pb:Br stoichiometric ratio is analyzed to be ~2:6, in agreement with the composition revealed by SCXRD (Fig. S4, ESI†). Raman spectra were further employed to confirm the structure (Fig. S5, ESI†). The well resolved Raman peaks at 60 and 77 cm^{-1} are assigned to the bending vibrations of the Br–Pb–Br bonds, and the sharp peaks located at 116 and 135 cm^{-1} are ascribed to the asymmetric and symmetric stretching vibrations of the Pb–Br bonds.[25,26] Moreover, the rigidity of the face-sharing bonding contributes to the strong peak intensity, different from the 3D ABX_3-type perovskite that exhibits broad un-resolved Raman peaks.[27]

Optical characterization was then conducted to survey the photophysical properties of (HM)Pb_2Br_6. The absorption spectrum reveals a distinct excitonic absorption with a sharp absorption edge at 390 nm (Fig. 2a). The band gap was calculated to be 3.05 eV based on the diffuse-reflectance spectrum (Fig. S6, ESI†). Moreover, the photoluminescence (PL) spectrum displays a broadband emission peaking at 692 nm upon 376 nm excitation, with a large Stokes shift of 302 nm and FWHM of 174 nm. The PLQY was measured to be 6.24%, much higher than that of the reported 1D lead bromide red emitter.[21] The Commission Internationale de l'Eclairage (CIE) chromaticity coordinates of the red emission were analysed to be (0.557, 0.3991) (Fig. 2b). Moreover, the correlated colour temperature (CCT) and colour purity were calculated to be 1698 K and 87%.

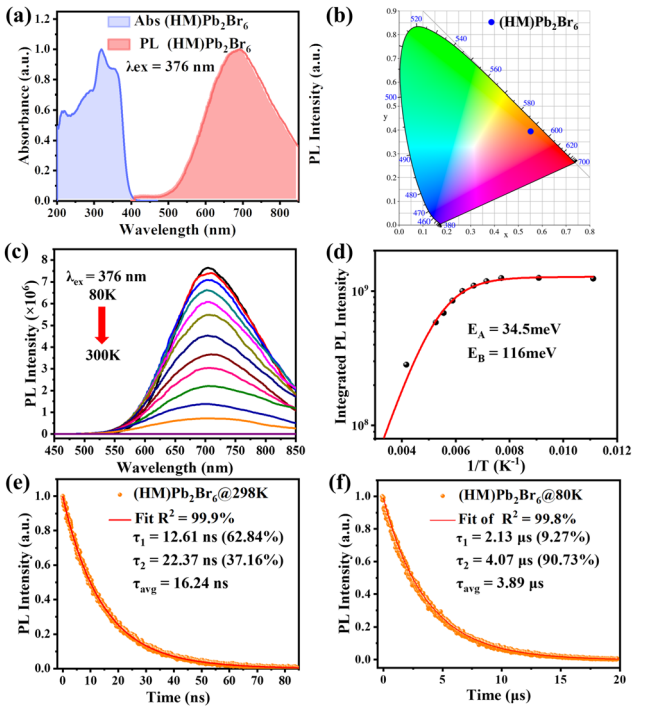

Fig. 2 (a) Normalized absorption and PL spectra of (HM)Pb_2Br_6. (b) The CIE 1931 chromaticity coordinate. (c) Temperature-dependent PL spectra of (HM)Pb_2Br_6. (d) Integrated PL intensity as a function of reciprocal temperature. Time-resolved PL decay curve of (HM)Pb_2Br_6 under a 375 nm excitation laser line at (e) 298 K and (f) 80 K.

Systematic spectroscopic investigations were then conducted to survey the origin of the red emission. Temperature-dependent PL spectra were firstly employed to investigate the evolution of the PL characters. As shown in Fig. 2c, the emission displays an obvious blue shift and increasing intensity as the temperature decreases from 298 to 80 K. At 80 K corresponding to low thermal activation, all excitons are located at self-trapped states and thus result in Stokes-shifted broadband emission. Moreover, the FWHM narrows from 174 to 137 nm with the decrease of the temperature, derived from the decreased nonradiative relaxation and enhanced electron–phonon coupling.[28] The integrated PL intensity as a function of temperature well agrees with the classical Arrhenius-type behavior,[29] which reveals two nonradiative thermally activated channels associated with two activation energies. The experimental data is then fitted with eqn (3) to deduce the activation energies, where I(T) and I_0 are the integrated PL intensities at temperature T and 0 K, A and B stand for the pre-exponential amplitudes, and E_A and E_B signify the activation energies.

$$I(T) = \frac{I_0}{1 + A e^{-E_A/k_B T} + B e^{-E_B/k_B T}} \quad (3)$$

The fitting yields an adjusted R^2 value of 0.99, extracting activation energies of E_A = 34.5 meV and E_B = 116 meV (Fig. 2d). The low E_A related with the non-dominant channels can be assigned as the detrapping process from the self-trapped excitons (STEs) to the free excitons (FEs). The high E_B is associated with the fast PL quenching, relating with the phonon modes involving the organic molecules.[24] Time-resolved PL spectra were then performed to survey the nature of the STEs. At 300 K, the decay curve of $(HM)Pb_2Br_6$ shows a bi-exponential feature with lifetimes of 12.61 ns (62.84%) and 22.37 ns (37.16%) (Fig. 2e). The PL decay lifetime increases to 2.13 μs (9.27%) and 4.07 μs (90.73%) at 80 K (Fig. 2f), indicating the inhibition of the thermally activated de-trapping mechanism of STEs and non-radiative recombination.

PL measurements were then performed on both bulk single crystals and μm-sized powders to clarify the emission origin. The single crystals and powder show identical emission (Fig. 3a), excluding the possible photoemission origin from the surface defect states. Actually, the emissions deriving from the surface defects of crystals are largely dominated by the particle size and their aggregation.[30] The excitation light density dependent PL intensity was further conducted to confirm the emission origin. The emission intensity displays a near linear dependence on the excitation light intensity up to 2.7 kW cm^{-2} under 375 nm illumination (Fig. 3b and Fig. S8, ESI†), ruling out the permanent defect-dominated emission mechanism. These observations conform to the STEs emission characteristics.[17] There is no overlap among the absorption, PLE and PL spectra of $HMBr_2$ and $(HM)Pb_2Br_6$ (Fig. 3c), suggesting that no energy transfer occurs in this system. Moreover, the emission of $HMBr_2$ just extends to 600 nm, indicating negligible contribution to the broadband red emission. Moreover, the PL lifetime of $(HM)Pb_2Br_6$ (τ_{avg} = 16.24 ns) is longer than $HMBr_2$ (τ_{avg} = 0.82 ns) (Fig. 3d), excluding the emission

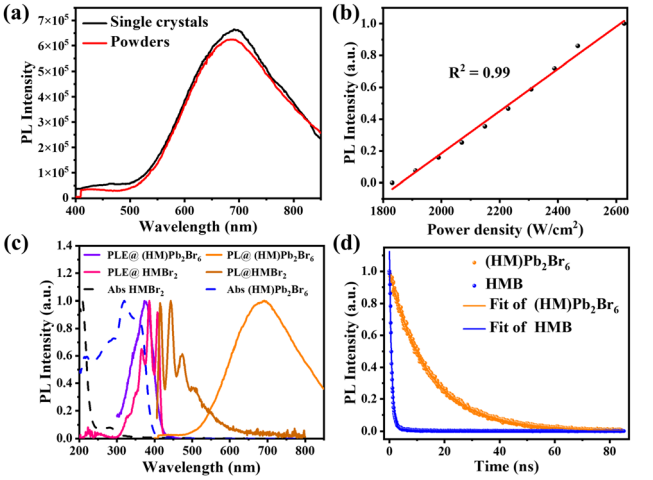

Fig. 3 (a) PL spectra of $(HM)Pb_2Br_6$ crystals and powder. (b) Integrated emission intensity *versus* excitation power for $(HM)Pb_2Br_6$. (c) Normalized absorption, PLE and PL spectra of $HMBr_2$ and $(HM)Pb_2Br_6$. (d) Time-resolved PL lifetime of $(HM)Pb_2Br_6$ and $HMBr_2$ under 375 nm excitation at 298 K.

origin from $HMBr_2$. The XRD pattern of the $(HM)Pb_2Br_6$ crystals shows negligible changes after storing in air for 6 months and illuminating under a 300 W UV lamp for 6 h, indicating high structure stability. And the PL intensity of the $(HM)Pb_2Br_6$ crystals displays slight degradation after storage for 6 months in air and illuminating for 6 h.

Density functional theory (DFT) calculations were then employed to investigate the attribute of STEs. The electronic structure and density of states (DOS) calculations show that the valence band maximum (VBM) and conduction band minimum (CBM) are consisted of antibonding states of Br 4p and Pb 6s (Pb 6p) (Fig. 4a and b). The CB has negligible dispersion perpendicular to the 1D chain, indicating strong confinement of excitons in the inorganic chain. In view of the shortened Pb–Pb and Br–Br distances, we expect the formation of Pb_2^{3+}, Pb_3^{+} and Br_2^{-} color centers in the lead bromide framework.[24] Accordingly, the DFT-PBE calculations of the charge density

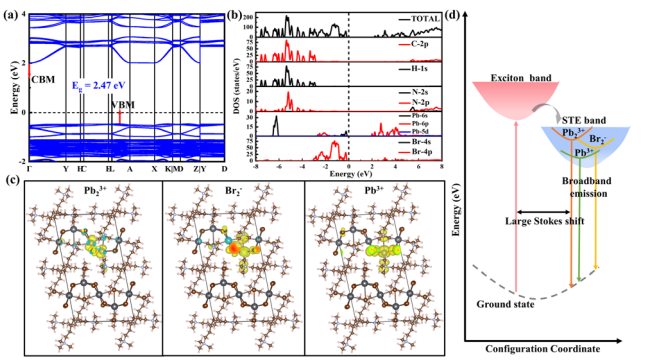

Fig. 4 (a) Calculated electronic band structures and (b) DOS of $(HM)Pb_2Br_6$. (c) Calculated charge density for $(HM)Pb_2Br_6$ (Pb_2^{3+} STELs, Br_2^{-} and Pb^{3+} STHLs holes) upon crystal lattice perturbation *via* the Pb–Pb, Br–Br and Pb–Br distances shortening. (d) Configuration coordinate diagram illustrating the luminescence mechanism.

distributions for dimerized Pb_2^{3+} self-trapped electrons (STELs) and dimerized Br_2^- and Pb_3^+ self-trapped holes (STHLs) were then conducted to identify the nature of the emissive states, where dimerization has been regarded as a perturbation in the lattice. Specifically, the 1D perovskite supercell models were built for exerting local perturbations, where selective bond lengths of Pb–Pb, Pb–Br and Br–Br with approximately nearest distance were shortened to cause the local structural distortion. In the unperturbed structure, the charges are fully delocalized in the inorganic framework (Fig. S8, ESI†). The Pb–Pb dimerization drives selective localization of electron density close to the disturbed lattice sites (Fig. 4c), in agreement with the reported STELs at Pb_2^{3+} sites.[31] Besides, it is found that holes gets self-localized within Br–Br and Pb^{3+} sites as well, coupling with the lattice distortion driven by Pb–Br bond shortening around the localization site (Fig. 4c), yielding Br_2^- color centers. Moreover, the energy level of STELs is calculated to be higher than that of STHLs (Fig. S11, ESI†), thus resulting in the large Stokes shift (Fig. 4d).[32]

In summary, we have developed a novel 1D $(HM)Pb_2Br_6$ perovskitoid featuring a corrugated "3 × 3" chain, which causes high octahedral distortion and short Pb–Pb and X–X pairs. Emphatically, it shows distinct broadband red emission with large Stokes shift, yielding PLQY of 6.24%. Systematic spectroscopic and theoretical investigation reveals that Pb_2^{3+}, Pb^{3+} and Br_2^- species confined within the inorganic lattice function as the radiative centres.

This work was supported by the National Natural Science Foundation of China (Grant 21805075, 11975093), the National Key R&D Program of China (Grant No. 2019YFB1503500), the Program for Science and Technology Innovation Team in Colleges of Hubei Province (Grant T201901), the Educational Commission of Hubei Province of China (Grant D20211001), and the Hubei International Cooperation Project (Grant 2021EHB005).

Conflicts of interest

There are no conflicts to declare.

Notes and references

1 S. P. Senanayak, K. Dey, R. Shivanna, W. W. Li, D. Ghosh, Y. C. Zhang, B. Roose, S. J. Zelewski, Z. Andaji-Garmaroudi, W. Wood, N. Tiwale, J. L. MacManus-Driscoll, R. H. Friend, S. D. Stranks and H. Sirringhaus, *Nat. Mater.*, 2023, **22**, 216–224.
2 Y. Q. Sun, L. S. Ge, L. J. Dai, C. S. Cho, J. F. Orri, K. Y. Ji, S. J. Zelewski, Y. Liu, A. J. Mirabelli, Y. C. Zhang, J. Y. Huang, Y. S. Wang, K. Gong, M. C. Lai, L. Zhang, D. Yang, J. D. Lin, E. M. Tennyson, C. Ducati, S. D. Stranks, L. S. Cui and N. C. Greenham, *Nature*, 2023, **615**, 830–835.
3 Y. Zhang, Y. G. Zhang, Y. Y. Zhao, H. Jia, Z. W. Yang, B. P. Yin, Y. C. Wu, Y. P. Yi, C. Zhang and J. N. Yao, *J. Am. Chem. Soc.*, 2023, **145**, 12360–12369.
4 D. T. Moore, H. Sai, K. W. Tan, D. M. Smilgies, W. Zhang, H. J. Snaith, U. Wiesner and L. A. Estroff, *J. Am. Chem. Soc.*, 2015, **137**, 2350–2358.
5 D. H. Fabini, T. Hogan, H. A. Evans, C. C. Stoumpos, M. G. Kanatzidis and R. Seshadri, *J. Phys. Chem. Lett.*, 2016, **7**, 376–381.
6 W. T. Yang, X. L. Xiao, M. K. Li, J. R. Hu, X. F. Xiao, G. L. Tong, J. N. Chen and Y. B. He, *Chem. Mater.*, 2021, **33**, 4456–4464.
7 Z. K. Qi, Y. L. Chen, Y. Guo, X. L. Yang, H. Z. Gao, G. J. Zhou, S. L. Li and X. M. Zhang, *Chem. Commun.*, 2021, **57**, 2495–2498.
8 C. K. Zhou, H. R. Lin, M. Worku, J. Neu, Y. Zhou, Y. Tian, S. Lee, P. Djurovich, T. Siegrist and B. Ma, *J. Am. Chem. Soc.*, 2018, **140**, 13181–13184.
9 X. X. Wu, M. T. Trinh and X. Y. Zhu, *J. Phys. Chem. C*, 2015, **119**, 14714–14721.
10 M. D. Smith, A. Jaffe, E. R. Dohner, A. M. Lindenberg and H. I. Karunadasa, *Chem. Sci.*, 2017, **8**, 4497–4504.
11 Y. Peng, Y. P. Yao, L. N. Li, Z. Y. Wu, S. S. Wang and J. H. Luo, *J. Mater. Chem. C*, 2018, **6**, 6033–6037.
12 H. Luo, S. H. Guo, Y. B. Zhang, K. J. Bu, H. R. Lin, Y. Q. Wang, Y. F. Yin, D. Z. Zhang, S. Y. Jin, W. Q. Zhang, W. G. Yang, B. W. Ma and X. J. Lu, *Adv. Sci.*, 2021, **8**, 2100786.
13 L. N. Li, W. T. Wu, D. Li, C. M. Ji, S. S. Lin, M. C. Hong and J. H. Luo, *CCS Chem.*, 2022, **4**, 2491–2497.
14 G. C. Yu, F. Lin, K. Zhou, S. F. Fang, Y. M. Shi, W. Liu, H. L. Hu, B. W. Ma and H. R. Lin, *Chem. Mater.*, 2021, **33**, 5668–5674.
15 E. R. Dohner, A. Jaffe, L. R. Bradshaw and H. I. Karunadasa, *J. Am. Chem. Soc.*, 2014, **136**, 13154–13157.
16 D. Cortecchia, S. Neutzner, A. R. S. Kandada, E. Mosconi, D. Meggiolaro, F. De Angelis, C. Soci and A. Petrozza, *J. Am. Chem. Soc.*, 2017, **139**, 39–42.
17 Z. Yuan, C. K. Zhou, Y. Tian, Y. Shu, J. Messier, J. C. Wang, L. J. van de Burgt, K. Kountouriotis, Y. Xin, E. Holt, K. Schanze, R. Clark, T. Siegrist and B. W. Ma, *Nat. Commun.*, 2017, **8**, 14051.
18 J. C. Yu, J. T. Kong, W. Hao, X. T. Guo, H. J. He, W. R. Leow, Z. Y. Liu, P. Q. Cai, G. D. Qian, S. Z. Li, X. Y. Chen and X. D. Chen, *Adv. Mater.*, 2019, **31**, 1806385.
19 C. Y. Yue, C. Sun, D. Y. Li, Y. H. Dong, C. L. Wang, H. F. Zhao, H. Jiang, Z. H. Jing and X. W. Lei, *Inorg. Chem.*, 2019, **58**, 10304–10312.
20 O. Nazarenko, M. R. Kotyrba, S. Yakunin, M. Aebli, G. Raino, B. M. Benin, M. Worle and M. V. Kovalenko, *J. Am. Chem. Soc.*, 2018, **140**, 3850–3853.
21 Y. Lin, Z. Z. Yao, Y. F. Han, X. Fan and S. C. Xiang, *Inorg. Chem. Commun.*, 2021, **129**, 108622.
22 F. L. Zhou, S. T. Song, M. M. Lun, H. N. Zhu, K. Ding, S. N. Cheng, D. W. Fu and Y. Zhang, *J. Mol. Struct.*, 2021, **1239**, 130468.
23 H. R. Lin, C. K. Zhou, J. Neu, Y. Zhou, D. Han, S. Y. Chen, M. Worku, M. Chaaban, S. Lee, E. Berkwits, T. Siegrist, M. H. Du and B. W. Ma, *Adv. Opt. Mater.*, 2019, **7**, 1801474.
24 R. Gautier, F. Massuyeau, G. Galnon and M. Paris, *Adv. Mater.*, 2019, **31**, 1807383.
25 C. Quarti, G. Grancini, E. Mosconi, P. Bruno, J. M. Ball, M. M. Lee, H. J. Snaith, A. Petrozza and F. De Angelis, *J. Phys. Chem. Lett.*, 2014, **5**, 279–284.
26 R. S. Tobias, *J. Chem. Educ.*, 1979, **56**(5), A209.
27 O. Yaffe, Y. S. Guo, L. Z. Tan, D. A. Egger, T. Hull, C. C. Stoumpos, F. Zheng, T. F. Heinz, L. Kronik, M. G. Kanatzidis, J. S. Owen, A. M. Rappe, M. A. Pimenta and L. E. Brus, *Phys. Rev. Lett.*, 2017, **118**, 136001.
28 L. L. Mao, P. J. Guo, M. Kepenekian, I. Hadar, C. Katan, J. Even, R. D. Schaller, C. C. Stoumpos and M. G. Kanatzidis, *J. Am. Chem. Soc.*, 2018, **140**, 13078–13088.
29 B. Febriansyah, T. Borzda, D. Cortecchia, S. Neutzner, G. Folpini, T. M. Koh, Y. X. Li, N. Mathews, A. Petrozza and J. England, *Angew. Chem., Int. Ed.*, 2020, **59**, 10791–10796.
30 M. J. Bowers, J. R. McBride and S. J. Rosenthal, *J. Am. Chem. Soc.*, 2005, **127**, 15378–15379.
31 D. Cortecchia, J. Yin, A. Bruno, S. Z. A. Lo, G. G. Gurzadyan, S. Mhaisalkar, J. L. Bredas and C. Soci, *J. Mater. Chem. C*, 2017, **5**, 2771–2780.
32 J. L. Yin, Y. Yu, X. L. Song, Y. L. Jiang and H. H. Fe, *CCS Chem.*, 2022, **4**, 540–547.

